

Article

The Development of New Perovskite-Type Oxygen Transport Membranes Using Machine Learning

Hartmut Schlenz ^{1,2,3,*}, Stefan Baumann ^{1,3}, Wilhelm Albert Meulenberg ^{1,3,4} and Olivier Guillon ^{1,3,5}

¹ Forschungszentrum Juelich, Institute of Energy and Climate Research (IEK), IEK-1: Materials Synthesis and Processing, Wilhelm-Johnen-Strasse, D-52425 Juelich, Germany; s.baumann@fz-juelich.de (S.B.); w.a.meulenberg@fz-juelich.de (W.A.M.); o.guillon@fz-juelich.de (O.G.)

² Institute of Geoscience, Division of Geochemistry and Petrology, University of Bonn, Meckenheimer Allee 139, D-53115 Bonn, Germany

³ Juelich Aachen Research Alliance: JARA-Energy, D-52425 Juelich, Germany

⁴ Faculty of Science and Technology, Inorganic Membranes, University of Twente, P.O. Box 217, 7500 AE Enschede, The Netherlands

⁵ Department of Ceramics and Refractory Materials, Institute of Mineral Engineering, RWTH Aachen University, D-52064 Aachen, Germany

* Correspondence: h.schlenz@fz-juelich.de; Tel.: +49-2461-61-96956

† These authors contributed equally to this work.

Abstract: The aim of this work is to predict suitable chemical compositions for the development of new ceramic oxygen gas separation membranes, avoiding doping with toxic cobalt or expensive rare earths. For this purpose, we have chosen the system $(\text{Sr}_{1-x}\text{Ba}_x)(\text{Ti}_{1-y-z}\text{V}_y\text{Fe}_z)\text{O}_{3-\delta}$ (cubic perovskite-type phases). We have evaluated available experimental data, determined missing crystallographic information using bond-valence modeling and programmed a Python code to be able to generate training data sets for property predictions using machine learning. Indeed, suitable compositions of cubic perovskite-type phases can be predicted in this way, allowing for larger electronic conductivities of up to $\sigma_e = 1.6 \text{ S/cm}$ and oxygen conductivities of up to $\sigma_i = 0.008 \text{ S/cm}$ at $T = 1173 \text{ K}$ and an oxygen partial pressure $p_{\text{O}_2} = 10^{-15} \text{ bar}$, thus enabling practical applications.

Keywords: ceramic; perovskite; oxygen separation membrane; mixed ionic-electronic conducting membrane MIEC; valence bond calculations; machine learning; python programming; Pecon.py

PACS: 02.60.-x; 02.60.DC; 02.60.Ed; 02.70.-c; 31.15.xw; 51.20.+d; 51.50.+v; 61.43.-j; 61.50.-f; 61.50.Ah; 61.66.-f; 61.66.Fn; 61.72.U-; 65.40.gk; 66.10.Ed; 66.30.je; 72.60.+g; 72.80.-r; 72.22.-d; 81.05.Je; 81.05.Zx; 82.33.Pt; 82.45.Un; 82.45.Xy; 82.47.-a



Citation: Schlenz, H.; Baumann, S.; Meulenberg, W.A.; Guillon, O. The Development of New Perovskite-Type Oxygen Transport Membranes Using Machine Learning. *Crystals* **2022**, *12*, 947. <https://doi.org/10.3390/cryst12070947>

Academic Editor: Maria Gazda, Shujun Zhang

Received: 9 April 2022

Accepted: 7 June 2022

Published: 5 July 2022

Publisher's Note: MDPI stays neutral with regard to jurisdictional claims in published maps and institutional affiliations.



Copyright: © 2022 by the authors. Licensee MDPI, Basel, Switzerland. This article is an open access article distributed under the terms and conditions of the Creative Commons Attribution (CC BY) license (<https://creativecommons.org/licenses/by/4.0/>).

1. Introduction

Mixed ion-electronically conducting ceramic-based membranes (MIEC) for oxygen separation have been synthesized and characterized for more than 30 years, mainly based on perovskite-type structures [1–8], such as $\text{SrTi}_x\text{Fe}_{1-x}\text{O}_{3-\delta}$ [9] and $\text{Ba}_{0.5}\text{Sr}_{0.5}\text{Co}_{0.8}\text{Fe}_{0.2}\text{O}_{3-\delta}$ [10,11]. Oxygen transport in dense ceramic membranes is driven by the partial pressure gradient across the membrane [9,12,13]. As mixed conducting materials single-phase perovskite can be used. Based on SrTiO_3 (STO), materials with the general structural formula ABO_3 offer a range of uses as functional materials in a variety of energy applications. For example, pure STO is used as a dielectric in electronic components. The crystal structure allows for a large number of dopants, making it possible to selectively introduce conductivities for electrons and/or oxygen ions into the material. Functionalized and doped STO materials are therefore used, e.g., as thermoelectrics, in the photovoltaic industry as well as in ceramic fuel cells or as gas separation membranes (high electronic and ionic conductivity) [12]. At the same time, the STO host lattice offers high intrinsic stability, which enables true long-term operation. As an example, dopants with Ba (A-position in the crystal structure) and

V/Fe (B-position) are selected and a methodology combining available experimental data, chemical bond modeling, and machine learning is developed. Doping with toxic Co will be deliberately avoided, as well as the use of rare earths (La, Ce, Sm), in order to keep production costs as low as possible. The properties of the chemical bonds and the resulting electron density distributions are decisive for the functional properties. Therefore, these are modeled using the bond valence method, as this requires significantly less computational power compared to ab initio methods (e.g., DFT) with similar information and provides faster results. In this way, screening of possible candidate materials is attainable, and oxygen diffusion as well as electronic conductivity can be optimized. However, there are frequent cases where ionic oxygen transport is accompanied by phase changes depending on temperature and oxygen partial pressure operating conditions. De Souza [14] published a comprehensive review of oxygen diffusion in undoped SrTiO₃ and related perovskite oxides that illustrates the relationship between defect chemistry, diffusion, and conductivity. There are some references regarding B-site substituted SrTiO₃ with V [15–17], but they are mainly related to the application of SrTiO₃-based ceramics such as thermoelectrics, solar cells, and sensors. However, such phases can also be used as stable gas separation membranes suitable for long-term application [6]. Doping of SrTiO₃ with Ba at the A position (ABO₃) enhances O₂ diffusion [6,18]. Inclusion of V at the B position increases electronic conductivity [6]. V⁵⁺ reduces an equivalent amount of Ti⁴⁺ to Ti³⁺, which in turn increases the electronic conductivity. As long as the cation radius of the dopant on the B side is smaller than that of Ti_{VI}⁴⁺ ($r_K = 0.605 \text{ \AA}$), the oxygen conductivity is always increased [14]. In fact, this is the case for V_{VI}⁴⁺ ($r_K = 0.580 \text{ \AA}$), V_{VI}⁵⁺ ($r_K = 0.540 \text{ \AA}$), and Fe_{VI}³⁺ ($r_K = 0.55 \text{ \AA}$), but not for Fe_{VI}²⁺ ($r_K = 0.610 \text{ \AA}$) (ionic radii: Shannon and Prewitt [19]). Here, Fe²⁺ and Fe³⁺ are assumed to be low-spin on the octahedral sites in the perovskite crystal structure. Experimentally determined cell constants of SrTi_xFe_{1-x}O_{3-δ} phases deliver strong evidence for this assumption, because cell constants clearly decrease with increasing iron content [9]. With relatively low doping with V crystal structure stability is maintained. The Ti-O and V-O bonds are almost equally strong, i.e., the incorporation of V does not affect the BO₆ network, which largely determines the stability of the perovskite structure, and V+Ti generally increases temperature stability, that can be estimated by calculating a tolerance factor t [6]. This factor is defined as $t = (r_A + r_O) / \sqrt{(r_B + r_O)}$ and for a stable structure t should be equal to 1.0. Bond-valence modeling (BVM) can be used to calculate stable compositions in advance before synthesis, hence saving a lot of time. One scientific goal of this project is to develop a better understanding of the relationship between chemical composition, tolerance factor t , critical radius r_c , the free volume FV in the crystal and in the micro structure, temperature T , and the binding energies of the metal–oxygen bonds. By combining available reference data and BVM for data supply, and subsequent machine learning (ML) for the prediction of promising chemical compositions, based on the supplied data, empirical trial-and-error methods will be avoided and a systematic way for the development of new ceramic ionic conductors will be established. Therefore, in this project structural parameters and conductivities of SrTiO₃, SrVO₃, Sr(Ti_{1-y}V_y)O₃, Sr(Ti_{1-z}Fe_z)O_{3-δ}, (Sr_{0.5}Ba_{0.5})(Ti_{0.5}Fe_{0.5})O_{3-δ}, (Sr_{1-x}Ba_x)(Ti_{1-y}V_y)O₃, and (Sr_{1-x}Ba_x)(Ti_{1-y-z}V_yFe_z)O_{3-δ} solid solutions, as a function of composition, temperature, and oxygen partial pressure were determined. The results are largely based on experimental data, and to a small extent on BVM. Conductivities are calculated, as far as possible, only for the practically relevant temperature range between 950 and 1223 K and oxygen partial pressures between 1 and 10⁻²⁰ bar (depending on composition).

2. Materials and Methods

2.1. Experimental Reference Data

Even if data are available (listed in Table 1), they are limited in temperature and/or oxygen partial pressure in most cases. Because no experimental values for oxygen conductivities are available for SrVO₃, and just for electronic conductivities, calculations were related to SrTiO₃, O–O bond lengths (1. order), and the free volume. For Sr(Ti_{1-y}V_y)O₃

also no experimental values for oxygen conductivities are available, just for electronic conductivities, and only at $T = 1173$ K. Therefore, calculations are also related to SrTiO_3 , O-O bond lengths (1. order), and the free volume (FV). In case of $\text{Sr}(\text{Ti}_{1-z}\text{Fe}_z)\text{O}_{3-\delta}$ conductivity data are only available at $T = 1123$ K for the whole compositional range, and especially conductivity data are available at $T = 973$ to 1223 K for $z = 0.4$ to 0.8 . Here, the space group is $Pm - 3m$ even up to $z = 0.8$. Only data for oxidizing conditions ($p\text{O}_2 = 0.213$ bar) are available. For compositions containing the cations Sr, Ba, Ti, and Fe only data for the specific composition $(\text{Sr}_{0.5}\text{Ba}_{0.5})(\text{Ti}_{0.5}\text{Fe}_{0.5})\text{O}_{3-\delta}$ are available and only data for oxidizing conditions ($p\text{O}_2 = 0.213$ bar). For the two compositions $(\text{Sr}_{1-x}\text{Ba}_x)(\text{Ti}_{1-y}\text{V}_y)\text{O}_3$ and $(\text{Sr}_{1-x}\text{Ba}_x)(\text{Ti}_{1-y-z}\text{V}_y\text{Fe}_z)\text{O}_{3-\delta}$ no experimental data are available at all. Therefore, cell constants and tolerance factors were calculated using BVM (see following section), and only reducing conditions were considered. A first evaluation and analysis of the experimental data was performed with the statistical program R (<https://www.r-project.org>, accessed on 1 April 2022), in order to detect outlier data and to select the most precise and accurate reference data. The finally applied reference data are taken from the references [8,9,14,16,17,20–33].

Table 1. Availability of experimental electronic conductivity data σ_e and ionic conductivity data σ_i , respectively. For more details see Appendix A.

Composition	σ_e	σ_i
SrTiO_3	YES	YES
SrVO_3	YES	NO
$\text{Sr}(\text{Ti}_{1-y}\text{V}_y)\text{O}_3$	YES	NO
$\text{Sr}(\text{Ti}_{1-z}\text{Fe}_z)\text{O}_{3-\delta}$	YES	YES
$(\text{Sr}_{0.5}\text{Ba}_{0.5})(\text{Ti}_{0.5}\text{Fe}_{0.5})\text{O}_{3-\delta}$	YES	YES
$(\text{Sr}_{1-x}\text{Ba}_x)(\text{Ti}_{1-y}\text{V}_y)\text{O}_3$	NO	NO
$(\text{Sr}_{1-x}\text{Ba}_x)(\text{Ti}_{1-y-z}\text{V}_y\text{Fe}_z)\text{O}_{3-\delta}$	NO	NO

2.2. Bond-Valence Modeling

The bond-valence method (BVM) is a standard procedure for analyzing and validating crystal structures of inorganic materials [34–41]. BVM expresses the concept that bond lengths and bond valences are related, and that the sum of bond valences s_{ij} to an atom j is equal to its valence V_j . For an atom symmetrically coordinated by M similar atoms, the relationship is $s_{ij} = V_j/M$. If the bonds are not equal, a relationship between bond length and bond order is required, such as $s_{ij} = \exp[(d_0 - d_{ij})/b]$, where d_0 is the length of a single bond between atom j and atom i and d_{ij} is the actual distance [34–36]. The constant b is assumed to be 0.37 for most structures. The method is good at assigning oxidation states, and O_2 , OH, and H_2O can be distinguished. Possible H and Li positions can be predicted, and also conduction paths in ionic conductors [37–40]. Yamada et al. [42] recently showed that the structural stability of SrTiO_3 and CaTiO_3 can be calculated equally well by BVM and DFT. Inoue et al. [40] discovered a completely new family of oxide ionic conductors $\text{Ca}_{0.8}\text{Y}_{2.4}\text{Sn}_{0.8}\text{O}_6$ by the combined application of synchrotron powder diffraction experiments and BVM modeling. The SPuDS software [43,44] enables the prediction of perovskite-type crystal structures with BVM. Modeling was performed using the following strategy: Depending on composition one or two cations (Sr^{2+} , Ba^{2+}) were allowed on the A-site of the perovskite crystal structure, and additionally one, two, or three cations on the B-site (Ti^{4+} , V^{4+} , $\text{Fe}^{2+}/\text{Fe}^{3+}$). For a given temperature the correct space group was chosen (e.g., $Pm - 3m$ for SrTiO_3 at $T = 973$ K), the Glazer tilt system (e.g., $a0a0a0$ for SrTiO_3), and the fractions of the different cations on the two possible sites, respectively. Because no oxidizing conditions were relevant in this work for solid solutions containing vanadium, no V^{5+} was considered. Cation ordering on the B-site was allowed, as well as a variation of the average B-site volume. Tilt angles were not pre-defined, but were refined during modeling. Calculated values (as a function of temperature) were for example the global

instability index GII , the tolerance factor t , the tilt angle, the bond valence sum for each ion, and the lattice parameters. The lattice parameters and the tolerance factor were used as input for the program Pecon.py, which is described in the following section. For detailed definitions of the parameters mentioned above see references [43,44].

2.3. Data Analysis and Python Programming

Reference data were analyzed using the new python program Pecon.py (short form of **Perovskite conductivity**). With this program the structural parameters and conductivities of the pure perovskite-type phases and the solid solutions of interest SrTiO_3 , SrVO_3 , $\text{Sr}(\text{Ti}_{1-y}\text{V}_y)\text{O}_3$, $\text{Sr}(\text{Ti}_{1-z}\text{Fe}_z)\text{O}_{3-\delta}$, $(\text{Sr}_{0.5}\text{Ba}_{0.5})(\text{Ti}_{0.5}\text{Fe}_{0.5})\text{O}_{3-\delta}$, $(\text{Sr}_{1-x}\text{Ba}_x)(\text{Ti}_{1-y}\text{V}_y)\text{O}_3$, and $(\text{Sr}_{1-x}\text{Ba}_x)(\text{Ti}_{1-y-z}\text{V}_y\text{Fe}_z)\text{O}_{3-\delta}$ can be calculated as a function of composition, temperature, and oxygen partial pressure. The results are largely based on fits and interpolation of analyzed, experimental data [8,9,14,16,17,20–33], and to a small extent on bond-valence modeling. Electronic and oxygen ion conductivities are calculated, as far as possible, only for the practically relevant temperature range between $T = 950$ to 1223 K (depending on composition). Appendix A shows the input that has to be given by the user: Chemical composition (characterized by three dimensionless variables x , y and z), temperature (K), and the oxygen partial pressure (bar). If the input parameters are outside pre-defined limits, the user receives an error message. Based on the user input Pecon.py calculates the space group and the related crystal data (cell constants, volume of the unit cell, atomic number density, bond lengths, and inter atomic distances). Additionally, the tolerance factor is calculated for the chosen temperature, as well as three conductivities (total, electronic, and ionic). Furthermore, parameter values that are related to conductivity are given (critical radius, free volume, and oxygen diffusion saddle point [20]). For this purpose within the program Pecon.py the data are fitted with polynomials of 2nd to 4th degree, or with exponential functions. Only interpolations between known data boundaries take place, but no extrapolations. Only experimental data were considered and no results from quantum mechanics (e.g., DFT) or other sources. Gaps of structural data (especially cell constants and tolerance factors) were filled with results achieved using BVM, as described above. All results calculated by Pecon.py are written to separate text files, which can be further used. One application is the generation of training data sets, that can be used for subsequent machine learning simulations (see following section). The detailed use of Pecon.py is shown in Appendix A and possible results are given in Appendix B.

2.4. Machine Learning

The training data set, that was generated using Pecon.py contained 26,916 data points, where each data point consists of 15 numerical values, for the pure phases and solid solutions mentioned above. The parameters used for machine learning are: T (K) (Temperature), r_A (Å) (Average ionic radius on the A-site), r_B (Å) (Average ionic radius on the B-site), $\log_{10} p\text{O}_2$ (bar) (logarithm of oxygen partial pressure), V_{uc} (Å³) (Volume of the unit cell), N (atoms/Å³) (Atomic number density), r_{BO} (Å) (B-O bond length), r_{AO} (Å) (A-O bond length), r_{BB} (Å) (B-B inter atomic distance), r_{AB} (Å) (A-B interatomic distance), t (Tolerance factor), r_c (Å) (Critical radius), FV (Å³) (Free volume), σ_e (S/cm) (Electronic conductivity), and σ_i (S/cm) (Ionic conductivity) (see also Appendix B). The chosen parameters are suitable for the sufficient characterization of the crystal structures and the respective dependencies of the conductivities on these structures. Missing conductivity (electronic and ionic) values of SBTVO and SBTVFO were marked accordingly in the training dataset. We used the most recent stable version 3.8.6 of the WEKA data mining tool kit [45,46], that can be used very well for supervised machine learning with numerical data. Simulations were performed on a single Linux-Workstation (Ubuntu 20.04 LTS, Intel i9, 20 cores, 64 GB RAM, Nvidia graphics card GeForce RTX 3080 (3000 cores, 10 GB RAM), 2 SSD (2 TB each)). As part of the WEKA package we used the Explorer program, which is suitable for preprocessing the data, for the application of chosen classifiers (training and testing) and for the visualization of the simulation results (predictions), respectively. We have tried

various classifiers such as SVM empirically, but we also used Auto-WEKA [47], in order to find the most suitable classifiers automatically. It turned out, that for the electronic conductivities lazy.IBK (K-nearest neighbour classifier [48]) can provide the most reasonable predictions. Therefore, with lazy.IBK we performed ML applying cross-validation (20 folds). The predicted values served as additional input for the training dataset. Afterwards, we searched for the best classifier even for the ionic conductivities as described above, using the modified training data. In this case a support-vector machine turned out to be the best choice for the prediction, using a radial basis function as kernel-type [49,50]. Correlation coefficients were 1.0 (σ_e) and 0.9962 (σ_i), mean absolute errors 0.0452 (σ_e) and 0.0005 (σ_i), and finally the relative absolute errors were 0.0671% for σ_e predictions and 2.1164% for the σ_i predictions. Selected results for the pure phases and some relevant compositions are listed in Table 2. Figure 1 demonstrates the workflow applied in this work.

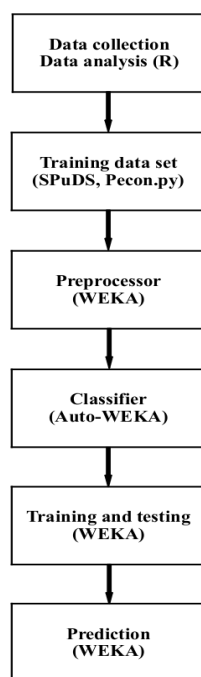


Figure 1. The workflow applied in this work, using the programs R, SPuDS, Pecon.py, WEKA, and Auto-WEKA, respectively.

Table 2. Predicted electronic and ionic (oxygen) conductivities σ_e and σ_i at $T = 1173$ K, respectively.

Composition	pO_2 (bar)	FV (\AA^3)	σ_e (S/cm)	σ_i (S/cm)
SrTiO ₃	1.0×10^{-15}	16.011	1.67×10^{-2}	2.51×10^{-5}
SrVO ₃	1.0×10^{-15}	13.377	545.09	2.27×10^{-5}
Sr(Ti _{0.5} V _{0.5})O ₃	1.0×10^{-15}	15.320	20.01	1.22×10^{-4}
Sr(Ti _{0.5} Fe _{0.5})O _{3-δ}	0.213	13.360	1.67	0.05
(Sr _{0.5} Ba _{0.5})(Ti _{0.5} Fe _{0.5})O _{3-δ}	0.213	17.904	1.56	0.13
(Sr _{0.5} Ba _{0.5})(Ti _{0.8} V _{0.1} Fe _{0.1})O _{3-δ}	1.0×10^{-15}	16.729	1.60	6.94×10^{-3}
(Sr _{0.5} Ba _{0.5})(Ti _{0.7} V _{0.1} Fe _{0.2})O _{3-δ}	1.0×10^{-15}	16.827	1.59	7.04×10^{-3}
(Sr _{0.5} Ba _{0.5})(Ti _{0.7} V _{0.2} Fe _{0.1})O _{3-δ}	1.0×10^{-15}	16.654	1.60	6.38×10^{-3}
(Sr _{0.5} Ba _{0.5})(Ti _{0.6} V _{0.3} Fe _{0.1})O _{3-δ}	1.0×10^{-15}	16.585	1.60	5.99×10^{-3}
(Sr _{0.5} Ba _{0.5})(Ti _{0.6} V _{0.2} Fe _{0.2})O _{3-δ}	1.0×10^{-15}	16.757	1.59	6.93×10^{-3}
(Sr _{0.5} Ba _{0.5})(Ti _{0.6} V _{0.1} Fe _{0.3})O _{3-δ}	1.0×10^{-15}	17.149	1.59	7.71×10^{-3}
(Sr _{0.5} Ba _{0.5})(Ti _{0.5} V _{0.3} Fe _{0.2})O _{3-δ}	1.0×10^{-15}	16.678	1.60	6.59×10^{-3}
(Sr _{0.5} Ba _{0.5})(Ti _{0.5} V _{0.2} Fe _{0.3})O _{3-δ}	1.0×10^{-15}	16.860	1.59	7.10×10^{-3}

3. Results

Figure 2 shows the electronic conductivity of STO, that is typically low for a dielectric material. The line in this figure has been calculated with Pecon.py, whereas the points are predicted by ML using WEKA. Please note, that the line does not represent a fit to the points, but is achieved independently. It can be clearly seen that the calculation and simulation provide an almost identical result.

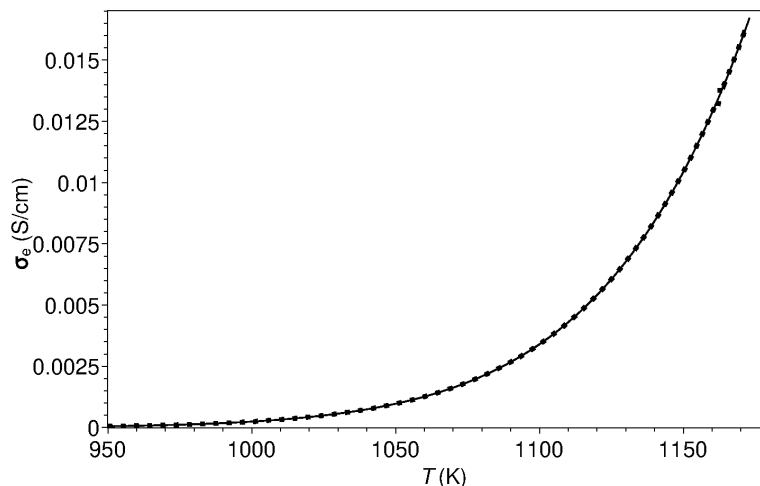


Figure 2. Electronic conductivity of SrTiO₃ at $pO_2 = 10^{-15}$ bar (Line: calculated by Pecon.py; Points: predicted by ML using WEKA).

In contrast, Figure 3 illustrates that pure SVO behaves like a metallic conductor, with an increasing electrical resistance with increasing temperature and the resulting decreased electronic conductivity. In the same temperature range, the electronic conductivity of SVO is several orders of magnitude larger than that of STO. The partial substitution of Ti by V on the B-site in the crystal structure of STVO increases the electronic conductivity significantly compared to STO (three orders of magnitude), but it still remains almost two orders of magnitude smaller than that of SVO (Figure 4). Compared to STVO the electronic conductivity of STFO is clearly decreased. Considering the same average cation radius $r_B = 0.6 \text{ \AA}$ for both phases, the electronic conductivity at $T = 1173 \text{ K}$ predicted for STVO is $\sigma_e = 0.47 \text{ S/cm}$ (Figure 4), whereas for STFO it is only $\sigma_e = 0.09 \text{ S/cm}$ (Figure 5).

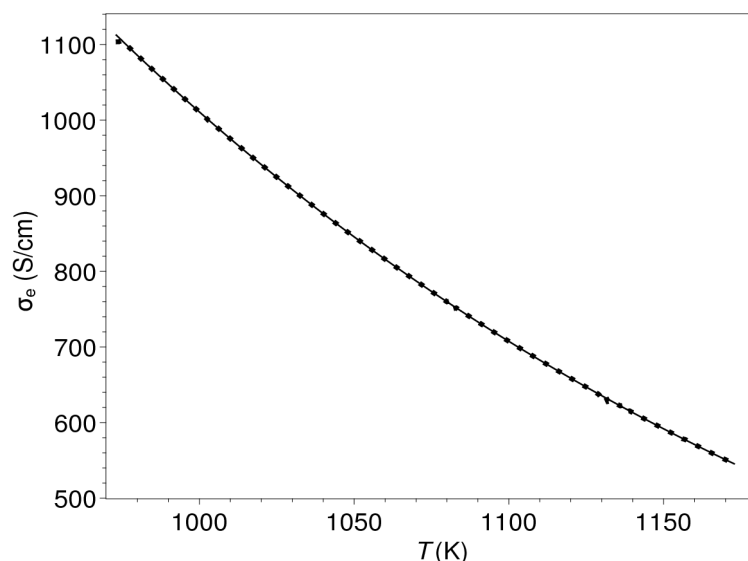


Figure 3. Electronic conductivity of SrVO₃ at $pO_2 = 10^{-15}$ bar (Line: calculated; Points: predicted).

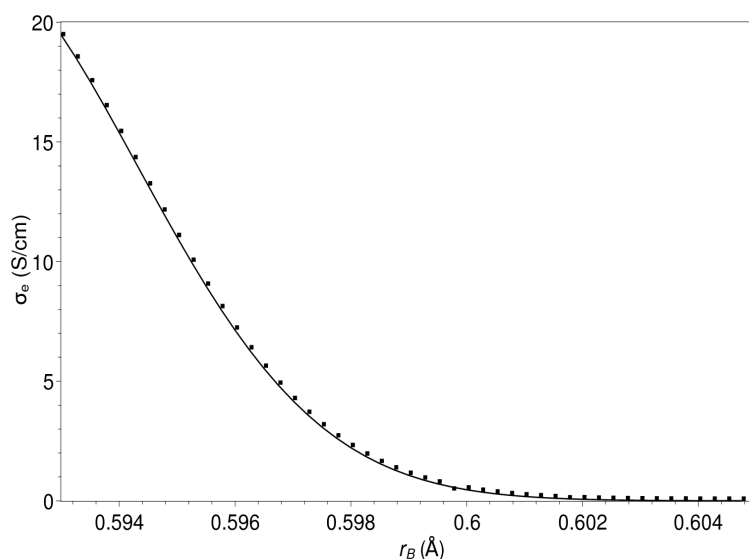


Figure 4. Electronic conductivity of $\text{Sr}(\text{Ti}_{1-y}\text{V}_y)\text{O}_3$ as a function of composition, expressed by the variable average cation radius on the B-site, corresponding to a y -range from 0.48 down to 0 (from left to right), at $T = 1173$ K and $p\text{O}_2 = 10^{-15}$ bar (Line: calculated; Points: predicted).

The partial substitution of Sr by Ba on the A-site in SBTFO decreases the electronic conductivity compared to STFO (Table 2), but at the same time the ionic conductivity is more than doubled. The ionic conductivity of STO is also very low (Figure 6) and here calculation and prediction are again almost identical. A first explanation is the substantially larger free volume (FV) within the crystal structure of SBTFO, a property that in many cases increases ionic conductivity under otherwise comparable conditions. Analogous to SVO, also for SBTFO a decrease in the electronic conductivity with increasing temperature can be observed (Figure 7), whereas the ionic conductivity increases with increasing temperature (Figure 8) as expected.

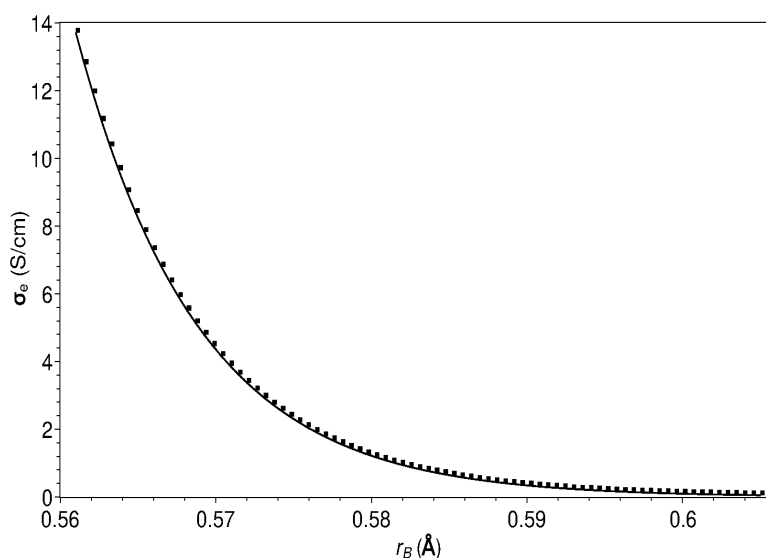


Figure 5. Electronic conductivity of $\text{Sr}(\text{Ti}_{1-z}\text{Fe}_z)\text{O}_{3-\delta}$ as a function of composition, expressed by the variable average cation radius on the B-site, corresponding to a z -range from 0.78 down to 0 (from left to right), at $T = 1173$ K and $p\text{O}_2 = 0.213$ bar (Line: calculated; Points: predicted).

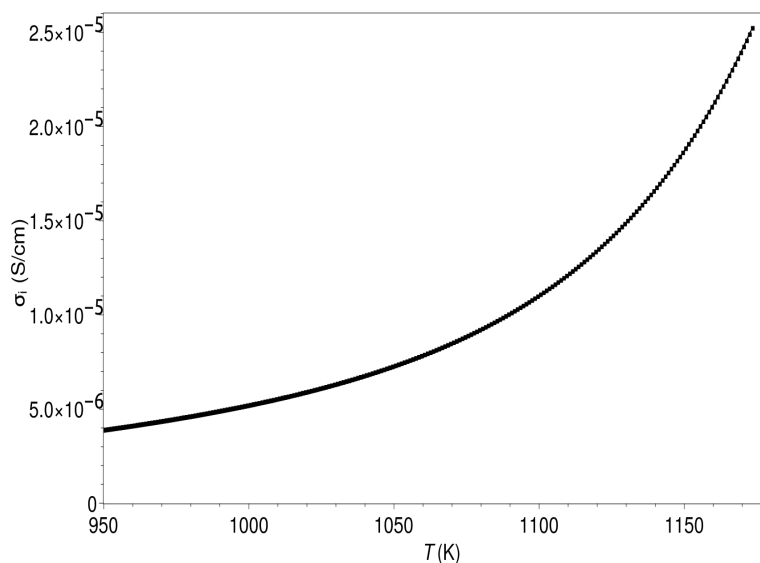


Figure 6. Ionic conductivity of SrTiO₃ at $pO_2 = 10^{-15}$ bar (Line: calculated; Points: predicted).

In summary, for all phases for which experimental conductivities are available (Table 1), the calculations with Pecon.py and the predictions using ML (WEKA) show a very good agreement, which in turn gives promise to a high reliability of the predictions for other similar phases, for which experimental data are missing. One important result to mention is the significant increase in the ionic conductivity due to the partial substitution of Sr by Ba on the A-site, especially compared to pure STO, in accordance to the results published by Teraoka et al. [18]. Table 2 summarizes selected, most promising compositions and the respective predictions of conductivities. Up to 50% Sr²⁺ can be substituted by Ba²⁺ on the A-site without phase transitions occurring and our predictions favor this larger Ba amount on the A-site in order to yield a larger ionic conductivity.

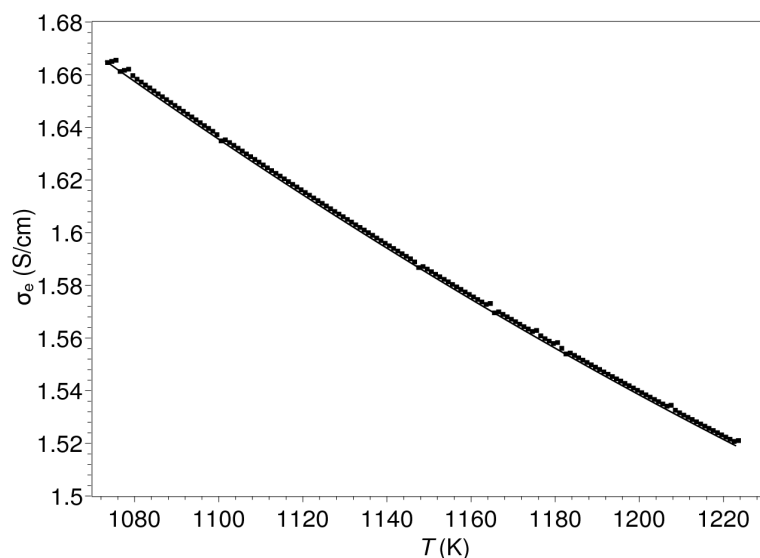


Figure 7. Electronic conductivity of $(Sr_{0.5}Ba_{0.5})(Ti_{0.5}Fe_{0.5})O_{3-\delta}$ at $pO_2 = 0.213$ bar (Line: calculated; Points: predicted).

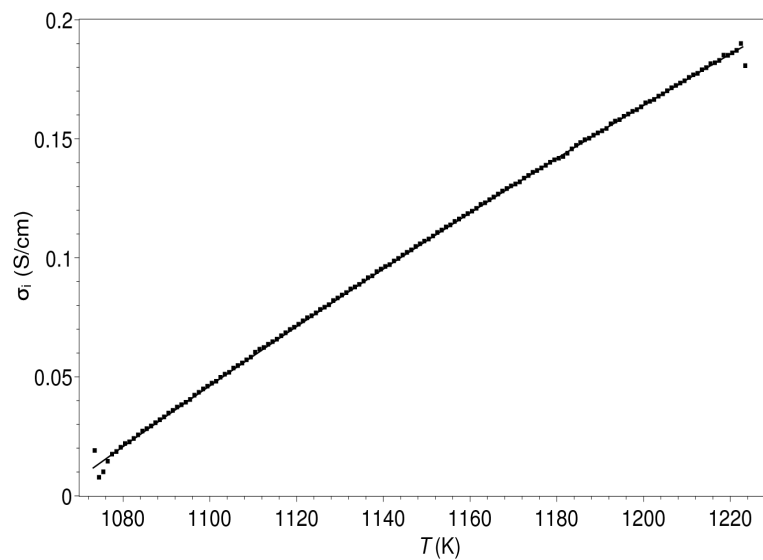


Figure 8. Ionic conductivity of $(\text{Sr}_{0.5}\text{Ba}_{0.5})(\text{Ti}_{0.5}\text{Fe}_{0.5})\text{O}_{3-\delta}$ at $p\text{O}_2 = 0.213$ bar (Line: calculated; Points: predicted).

4. Discussion

Compared to pure STO, the electronic and ionic conductivity can be increased by about two orders of magnitude due to doping with Ba on the A-site [18] and V/Fe on the B-site of the perovskite crystal structure, respectively. The predicted electronic conductivity remains nearly constant at values of about $\sigma_e \approx 1.6$ S/cm, independent of the given V/Fe ratio (Table 2), even without any V on the B-site. Unfortunately, V on the B-site reduces the ionic conductivity significantly compared to V-free phases. A key result of our work is, that a large electronic and a large ionic conductivity are not possible within the SBTVFO system at the same time. For MIEC membranes the ambivalent conduction is the figure of merit. Figure 9 shows a three-dimensional plot of both conductivities σ_e and σ_i related to the average cation radius r_B on the B-site for perovskite-type phases of composition $(\text{Sr}_{0.5}\text{Ba}_{0.5})(\text{Ti}_{1-y-z}\text{V}_y\text{Fe}_z)\text{O}_{3-\delta}$ at $p\text{O}_2 = 10^{-15}$ bar and $T = 1173$ K (see also Table 2). This plot shows the optimum values for all three parameters in order to yield large conductivities.

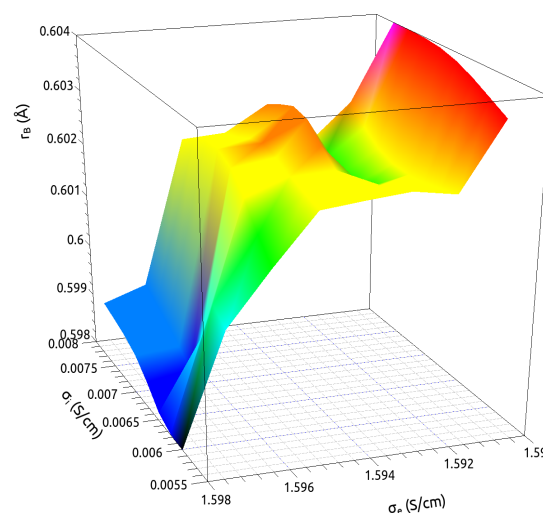


Figure 9. Figure of merit of the ambivalent conductivity of $(\text{Sr}_{0.5}\text{Ba}_{0.5})(\text{Ti}_{1-y-z}\text{V}_y\text{Fe}_z)\text{O}_{3-\delta}$ at $p\text{O}_2 = 10^{-15}$ bar and $T = 1173$ K (see text and Table 2).

Compared to SBTVFO achievable ionic conductivities with phases containing Co on the B-site are at least one order of magnitude larger. Perovskite-type phases containing 25 or 35 mole percent Co on the B-site achieve ionic conductivities in air at $T = 1123$ K of $\sigma_i = 0.022$ S/cm or $\sigma_i = 0.06$ S/cm, respectively, [16]. The incorporation of Co probably increases the mobility of oxygen vacancies and that is more important for larger ionic conductivities than the concentration of vacancies itself ([13], p. 185). However, the presence of V enables the operation at reducing conditions and keeps the material stable without any phase transformation. It generally remains difficult to replace Co and rare earths with other elements and still achieve comparable ionic conductivities. The electronic conductivities of Co-doped phases, however, are comparable to SBTVFO and of the same order. Thereby, the influence of the oxygen partial pressure on the electronic conductivities in the system SBTVFO seems to be rather small (Table 2). In the Fe-containing phases, on the other hand, the oxygen partial pressure plays a greater role. With decreasing values for pO_2 , the ionic conductivity also decreases significantly.

The method used in this work appears promising. The combination of available experimental data and easy to perform bond-valence model calculations, as well as subsequent machine learning, allows reasonable predictions of physical properties for similar ceramic phases, for which no corresponding experimental data are available. The applied experimental data result from the properties of the respective crystal structures and from the related micro structures. We see this as a clear advantage, since in this way all relevant material information becomes part of the training data sets used for machine learning. The training data set generated for this work with the new program Pecon.py is therefore based exclusively on such (combined) data. For the calculations in the program Pecon.py, as precise and accurate as possible basic crystallographic data are used as an essential component. Since bond lengths, inter-atomic distances, and the chemical bonds (as well as the resulting properties), do correlate directly with each other, it is essential to describe these input features as accurate as possible. Thus, we searched the literature for high quality, experimentally determined lattice constants to describe the unit cells. For STO, for example, we used the very precise and accurate data of Schmidbauer et al. [24].

In this work, we followed the main steps and strategies of ML in materials research, that is, sample representation by available experimental data and BVM, model building by regressions and classification, and finally model evaluation by cross-validation [51,52]. Butler et al. [53] have already pointed out that big data can also be, and often is, crucial in materials research using ML as a tool to achieve relevant and reasonable results. Especially in materials research, one often has to be satisfied with comparatively small data sets with a few hundred or thousand data points. Therefore, in this work we first tried to generate a sufficiently large data set for the investigated system in the first place by means of the new program Pecon.py. Alternatively, one can of course prefer DFT and the use of larger databases with predominantly DFT- and/or MD-simulated data to obtain ML training data [54–56], but often associated with a lack of accuracy for a specific system. We therefore followed a semi-empirical approach in this work, similar to the work of Xu et al. [57], with experimental data as the essential basis, combined with a deep analysis of the available data before they became part of the Pecon.py program and the resulting training data (Figure 1). We paid particular attention to structure-property relations [58] and limited ourselves to a maximum of five different pre-selected cations at the A and B positions, as well as two physical quantities to be predicted (electronic and ionic conductivity). Searching the periodic table for suitable chemical compositions was explicitly not our goal. In the same vein as other authors, we also see a clear advantage in the application of ML in materials research [59] and consider the linkage of ML and BVM, especially for ionic conductors to be particularly advantageous and promising [60], in order to achieve practically usable results in a relatively short time. Similar approaches, although not comparable in all aspects, have been followed in other work for the development of new perovskite phases in different application fields [61–68], sometimes using robotic technologies [69]. The sharing of available data is becoming increasingly important in order to continue to make progress

in the design and discovery of new perovskite-type phases [70–72]. In the future, structure-property relationships and their qualified evaluation will continue to play a large and important role [73,74], which is why we have also followed this approach.

A central concern of this work is to be able to predict, in the simplest possible way, the conductivities of ceramic oxygen membranes from a relatively small training data set of experimental values using ML. In doing so, it is hoped to encourage materials scientists who do not focus on simulations to use ML as a potential tool for their data analyses in the future. Another alternative approach may be the use of Artificial Neural Networks (ANN) for supervised learning in materials research [75,76]. ANN are a core component of deep learning and are useful for highly complex ML tasks, such as classification of billions of images, for speech recognition, or robotics. However, for an application in this work, effort and return are out of proportion. With a training data set of only about 27000 numerical records, simpler and faster regression methods for supervised learning are much more reasonable to use and also provide results much faster, since no neural networks have to be trained in advance. In contrast, the use of ANN requires significantly more know-how on the part of the user and the necessary infrastructure also makes higher demands. For the reasons mentioned above, we have chosen the simplest possible way to solve the task at hand and to demonstrate a practical example for the application of ML in materials research. Accordingly, the use of ANN is not envisaged in this work and will not be discussed further in detail, as such a discussion would go far beyond the focus of this work. For more extensive introductions to ANNs and their use, especially in materials research, we refer to some recent papers [77,78], among others.

5. Conclusions

Concluding, the presented approach enables the application of machine learning in materials research in a comparatively simple way. The infrastructure required for the implementation of this project was mainly limited to a powerful Linux workstation and the necessary freely available software (Python 3, R, SPuDS, WEKA, and finally QtiPlot (<https://qtiplot.com>, accessed on 1 April 2022) for the preparation of the presented graphs). Based on available reference data, some additional bond-valence calculations and the data analysis using the developed software Pecon.py enabled the generation of a consistent training data set. In this way, available experimental conduction data for the phases STO, SVO, STVO, STFO and SBTFO could be reproduced very well, and also reasonable predictions of the electronic and ionic conductivities of cubic perovskite-type ceramics $(\text{Sr}_{1-x}\text{Ba}_x)(\text{Ti}_{1-y-z}\text{V}_y\text{Fe}_z)\text{O}_{3-\delta}$ were possible, for which no experimental data are available. However, the maximum achievable conductivities are about one power of ten smaller than for Co- and REE-bearing phases ($\sigma_e = 1.6 \text{ S/cm}$, $\sigma_i = 0.008 \text{ S/cm}$ at $T = 1173 \text{ K}$ and $p_{\text{O}_2} = 10^{-15} \text{ bar}$, predicted for $(\text{Sr}_{0.5}\text{Ba}_{0.5})(\text{Ti}_{0.6}\text{V}_{0.1}\text{Fe}_{0.3})\text{O}_{3-\delta}$). Therefore, the SBTVFO system can not compete with established MIEC phases in this respect. It is thus not as promising as hoped, but could be used in dual-phase membranes as a predominantly electronic mixed conductor with a slight ionic conductivity, e.g., as part of a construction of so-called MIEC-MIEC composite membranes, which makes a practical application possible in any case. Regardless of this, the presented strategy could be adapted to similar phases and problems quite easily, without the need of prior and more sophisticated electronic structure methods such as density functional theory (DFT) or molecular dynamics simulations (MD). The latter could both be an alternative in some way, but they require a much greater effort than the strategy presented here, and they require significantly more time. Furthermore, the use of Artificial Neural Networks (ANN) is not really necessary here, as the effort required for this is also greater than for the demonstrated methods. ANNs make particular sense for significantly larger data sets and for real-time applications, neither of which is the case in this work.

Author Contributions: Conceptualization, H.S. and S.B.; methodology, H.S., S.B. and W.A.M.; software, H.S.; validation, H.S., S.B., W.A.M. and O.G.; formal analysis, H.S. and S.B.; investigation, H.S.; resources, H.S. and O.G.; data curation, H.S. and S.B.; writing—original draft preparation, H.S.; writing—review and editing, H.S., S.B., W.A.M. and O.G.; visualization, H.S.; supervision, W.A.M. and O.G.; project administration, H.S.; funding acquisition, H.S. All authors have read and agreed to the published version of the manuscript.

Funding: This research was funded by the Helmholtz Innovation Fund (Project No. DB001840).

Institutional Review Board Statement: Not applicable.

Informed Consent Statement: Not applicable.

Data Availability Statement: The Python source code of the program Pecon.py and the generated training data set are both available upon reasonable request from the corresponding author.

Acknowledgments: We thank the Helmholtz Association of German Research Centers and Forschungszentrum Juelich for providing the time and infrastructure necessary to perform the presented work.

Conflicts of Interest: The authors declare no conflicts of interest.

Abbreviations

The following abbreviations are used in this manuscript:

Auto-WEKA	Automatic Model Selection and Hyperparameter Optimization in WEKA
BVM	Bond Valence Model
CLI	Command Line Interface
DFT	Density Functional Theory
FV	Free Volume
lazy.IBK	K-nearest Neighbours (WEKA Classifier)
MD	Molecular Dynamics
ML	Machine Learning
pO_2	Oxygen Partial Pressure
SG	Space Group
SVM	Support Vector Machine (WEKA Classifier)
STO	SrTiO ₃
SVO	SrVO ₃
STVO	Sr(Ti _{1-y} V _y)O ₃
STFO	Sr(Ti _{1-z} Fe _z)O _{3-δ}
SBTFO	(Sr _{0.5} Ba _{0.5})(Ti _{0.5} Fe _{0.5})O _{3-δ}
SBTVO	(Sr _{1-x} Ba _x)(Ti _{1-y} V _y)O ₃
SBTVFO	(Sr _{1-x} Ba _x)(Ti _{1-y-z} V _y Fe _z)O _{3-δ}
WEKA	Waikato Environment for Knowledge Analysis

Appendix A

The program Pecon.py has a simple command line interface (CLI). The following lines show the screen output you will see in a terminal, when you start the program. The necessary command is `>python3 pecon.py` (independent of the used operating system):

Program PECON

Structural parameters and conductivities of SrTiO₃, SrVO₃, SrTi(1-y)V(y)O₃, SrTi(1-z)Fe(z)O₃, Sr(0.5)Ba(0.5)Ti(0.5)Fe(0.5)O₃, Sr(1-x)Ba(x)Ti(1-y)V(y)O₃, and Sr(1-x)Ba(x)Ti(1-y-z)V(y)Fe(z) solid solutions, as a function of composition, temperature and oxygen partial pressure.

The results are largely based on fits and interpolation of analyzed, experimental data, and to a small extent on bond-valence modeling. Conductivities are calculated, as far as possible, only for the practically relevant temperature range between 950 and 1223 K (depending on composition).

(c) Written by Hartmut Schlenz (2022), Python 3.8.8

Screen output is written to file pecon_*.out
 Complete results are saved as pecon_results_*.txt
 Graphics are saved as pecon_*.png

TEMPERATURE LIMITS:

Structure data:

SrTiO₃ -> $T = 0$ to 2313 K
 SrVO₃ -> $T = 0$ to 1956 K
 SrTi(1-y)V(y)O₃ -> $T = 973$ to 1173 K
 SrTi(1-z)Fe(z)O₃ -> $T = 973$ to 1173 K
 Sr(0.5)Ba(0.5)Ti(0.5)Fe(0.5)O₃ -> $T = 1073$ to 1223 K
 Sr(1-x)Ba(x)Ti(1-y)V(y)O₃ -> $T = 973$ to 1173 K
 Sr(1-x)Ba(x)Ti(1-y-z)V(y)Fe(z)O₃ -> $T = 973$ to 1173 K

Conductivities:

SrTiO₃ -> $T = 950$ to 1173 K
 SrVO₃ -> $T = 973$ to 1173 K
 SrTi(1-y)V(y)O₃ -> $T = 1173$ K
 SrTi(1-z)Fe(z)O₃ -> $T = 973$ to 1223 K
 Sr(0.5)Ba(0.5)Ti(0.5)Fe(0.5)O₃ -> $T = 1073$ to 1223 K
 Sr(1-x)Ba(x)Ti(1-y)V(y)O₃ -> $T =$ no data available
 Sr(1-x)Ba(x)Ti(1-y-z)V(y)Fe(z)O₃ -> $T =$ no data available

LIMITS OF OXYGEN PARTIAL PRESSURE:

SrTiO₃ -> $pO_2 = 1.0 \times 10^{-20}$ to 1.0 bar
 SrVO₃ -> $pO_2 = 1.0 \times 10^{-20}$ to 1.0×10^{-15} bar
 SrTi(1-y)V(y)O₃ -> $pO_2 = 1.0 \times 10^{-20}$ to 1.0×10^{-11} bar
 SrTi(1-z)Fe(z)O₃ -> $pO_2 = 0.213$ bar
 Sr(0.5)Ba(0.5)Ti(0.5)Fe(0.5)O₃ -> $pO_2 = 0.213$ bar
 Sr(1-x)Ba(x)Ti(1-y)V(y)O₃ -> $pO_2 = 1.0 \times 10^{-20}$ to 1.0×10^{-15} bar
 Sr(1-x)Ba(x)Ti(1-y-z)V(y)Fe(z)O₃ -> $pO_2 = 1.0 \times 10^{-15}$ bar

Input x -value equal 0.0 (no Ba²⁺ on the A-site) or > 0.0 and <= 0.5:

Input y -value equal 0.0 (SrTiO₃) or 1.0 (SrVO₃) or > 0.0 and <= 0.5 (SrTi(1-y)V(y)O₃):

Input z -value equal 0.0 (no Fe^{2+/3+} on the B-site) or > 0.0 and <= 0.5 or <= 0.8

(only SrTi(1-z)Fe(z)O₃):

Input temperature T (K):

Input oxygen partial pressure pO_2 (bar):

Appendix B

The following screen output shows the values that can be calculated for each phase, in this case for the pure dielectric SrTiO₃:

Program PECON—Results

Phase = SrTiO₃
 User input x = 0.000000
 User input y = 0.000000
 User input z = 0.000000
 User input T = 973.000000 K
 User input pO_2 = 1.000000×10^{-15} bar

Crystal data:

Cubic crystal structure	SG	=	$Pm - 3m$
Cell constant	a	=	3.918795 Å
Volume of the unit cell	V	=	60.180762 Å ³
Atomic number density	N	=	0.083083 atoms/Å ³
Tolerance factor	t	=	1.014169
O-O distance (1. order)		=	2.771007 Å
O-O distance (2. order)		=	3.918795 Å
Ti-O distance		=	1.959398 Å
Sr-O distance		=	2.771007 Å
Ti-Ti distance		=	3.918795 Å
Sr-Sr distance		=	3.918795 Å
Ti-Sr distance		=	3.393776 Å

Conductivities:

Critical radius	$r(c)$	=	0.895343 Å
Free volume	FV	=	15.827530 Å ³
O ₂ - diffusion saddle point	$ODSP$	=	0.439857
Total conductivity	$\Sigma(t)$	=	$1.1316857455 \times 10^{-4}$ S/cm
Electronic conductivity	$\Sigma(e^-)$	=	$1.0884879227 \times 10^{-4}$ S/cm
Oxygen conductivity	$\Sigma(O_2^-)$	=	$4.3197822829 \times 10^{-6}$ S/cm

In the background, the program additionally and automatically generates a training data set with the following parameters: T (K) (Temperature), r_A (Å) (Average ionic radius on the A-site), r_B (Å) (Average ionic radius on the B-site), $\log_{10} pO_2$ (bar) (logarithm of oxygen partial pressure), V_{uc} (Å³) (Volume of the unit cell), N (atoms/Å³) (Atomic number density), r_{TiO} (Å) (Ti-O bond length), r_{SrO} (Å) (Sr-O bond length), r_{TiTi} (Å) (Ti-Ti inter atomic distance), r_{TiSr} (Å) (Ti-Sr inter atomic distance), t (Tolerance factor), r_c (Å) (Critical radius), FV (Å³) (Free volume), σ_e (S/cm) (Electronic conductivity) and σ_i (S/cm) (Ionic conductivity) and graphs of the two conductivities. The step size for the temperature is 1 K and for the logarithm to base 10 of the oxygen partial pressure is equal 1. Thus, just for pure SrTiO₃, a data set is generated for the temperature range from $T = 950$ K to $T = 1173$ K with 4704 data points (lines) and a total of 70,560 numerical values.

References

- Deibert, W.; Ivanova, M.E.; Baumann, S.; Guillon, O.; Meulenberg, W.A. Ion-conducting ceramic membrane reactors for high-temperature applications. *J. Membr. Sci.* **2017**, *543*, 79–97. [[CrossRef](#)]
- Hashim, S.M.; Mohamed, A.R.; Bhatia, S. Current status of ceramic-based membranes for oxygen separation from air. *Adv. Colloid Interface Sci.* **2010**, *160*, 88–100. [[CrossRef](#)] [[PubMed](#)]
- Hashim, S.M.; Mohamed, A.R.; Bhatia, S. Oxygen separation from air using ceramic-based membrane technology for sustainable fuel production and power generation. *Renew. Sustain. Energy Rev.* **2011**, *15*, 1284–1293. [[CrossRef](#)]
- Hwang, J.; Rao, R.R.; Giordano, L.; Katayama, Y.; Yu, Y.; Shao-Horn, Y. Perovskites in catalysis and electrocatalysis. *Science* **2017**, *358*, 751–756. [[CrossRef](#)] [[PubMed](#)]
- Sunarso, J.; Baumann, S.; Serra, J.M.; Meulenberg, W.A.; Liu, S.; Lin, Y.S.; da Costa, J.C.D. Mixed ionic-electronic conducting (MIEC) ceramic-based membranes for oxygen separation. *J. Membr. Sci.* **2008**, *320*, 13–41. [[CrossRef](#)]
- Sunarso, J.; Hashim, S.S.; Zhu, N.; Zhou, W. Perovskite oxides applications in high temperature oxygen separation, solid oxide fuel cell and membrane reactor: A review. *Prog. Energy Combust. Sci.* **2017**, *61*, 57–77. [[CrossRef](#)]
- Ubic, R.; Tolman, K.; Chan, K.; Lundy, N.; Letourneau, S.; Kriven, W.M. Effective size of vacancies in aliovalently doped SrTiO₃ perovskites. *J. Alloys Compd.* **2013**, *575*, 239–245. [[CrossRef](#)]
- Ubic, R.; Tolman, K.; Talley, K.; Joshi, B.; Schmidt, J.; Faulkner, E.; Owens, J.; Papac, M.; Garland, A.; Rumrill, C.; et al. Lattice-constant prediction and effect of vacancies in aliovalently doped perovskites. *J. Alloys Compd.* **2015**, *644*, 982–995. [[CrossRef](#)]
- Schulze-Küppers, F.; ten Donkelaar, S.F.P.; Baumann, S.; Prigorodov, P.; Sohn, Y.J.; Bouwmeester, H.J.M.; Meulenberg, W.A.; Guillon, O. Structural and functional properties of SrTi_{1-x}Fe_xO_{3-δ} (0 ≤ x ≤ 1) for the use as oxygen transport membrane. *Sep. Purif. Technol.* **2015**, *147*, 414–421. [[CrossRef](#)]
- Unger, L.-S.; Niedrig, C.; Wagner, S.F.; Menesklou, W.; Baumann, S.; Meulenberg, W.A.; Ivers-Tiffée, E. Yttrium doping of Ba_{0.5}Sr_{0.5}Co_{0.8}Fe_{0.2}O_{3-δ} part I: Influence on oxygen permeation, electrical properties, reductive stability, and lattice parameters. *J. Eur. Ceram. Soc.* **2018**, *38*, 2378–2387. [[CrossRef](#)]

11. Unger, L.-S.; Ruhl, R.; Meffert, M.; Niedrig, C.; Menesklou, W.; Wagner, S.F.; Gerthsen, D.; Bouwmeester, H.J.M.; Ivers-Tiffée, E. Yttrium doping of $\text{Ba}_{0.5}\text{Sr}_{0.5}\text{Co}_{0.8}\text{Fe}_{0.2}\text{O}_{3-\delta}$ part II: Influence on oxygen transport and phase stability. *J. Eur. Ceram. Soc.* **2018**, *38*, 2388–2395. [[CrossRef](#)]
12. Meulenbergh, W.A.; Schulze-Küppers, F.; Deibert, W.; Van Gestel, T.; Baumann, S. Ceramic Membranes: Materials—Components—Potential Applications. *ChemBioEng Rev.* **2019**, *6*, 198–208. [[CrossRef](#)]
13. Zhu, X.; Yang, W. Perovskite-type MIEC membranes. In *Mixed Conducting Ceramic Membranes*; Springer: Berlin, Germany, 2017; pp. 179–226.
14. De Souza, R.A. Oxygen Diffusion in SrTiO_3 and Related Perovskite Oxides. *Adv. Funct. Mater.* **2015**, *25*, 6326–6342. [[CrossRef](#)]
15. Khan, T.T.; Mahmud, I.; Ur, S.-C. Synthesis and Thermoelectric Properties of the B-Site Substituted SrTiO_3 with Vanadium. *Korean J. Mater. Res.* **2017**, *27*, 416–421. [[CrossRef](#)]
16. Liu, Y.; Baumann, S.; Schulze-Küppers, F.; Mueller, D.N.; Guillon, O. Co and Fe co-doping influence on functional properties of SrTiO_3 for use as oxygen transport membranes. *J. Eur. Ceram. Soc.* **2018**, *38*, 5058–5066. [[CrossRef](#)]
17. Mantry, S.P.; Yadav, A.; Fahad, M.; Sarun, P.M. Effect of vanadium substitution on the dielectric and electrical conduction properties of SrTiO_3 ceramics. *Mater. Res. Express* **2018**, *5*, 036303. [[CrossRef](#)]
18. Teraoka, Y.; Nobunaga, T.; Yamazoe, N. Effect of Cation Substitution on the Oxygen Semipermeability of Perovskite-type Oxides. *Chem. Lett.* **1988**, *3*, 503–506. [[CrossRef](#)]
19. Shannon, R.D.; Prewitt, C.T. Effective Ionic Radii in Oxides and Fluorides. *Acta Cryst.* **1969**, *B25*, 925–946. [[CrossRef](#)]
20. Sammels, A.F.; Cook, R.F.; White, J.H.; Osborne, J.J.; MacDuff, R.C. Rational selection of advanced solid electrolytes for intermediate temperature fuel cells. *Solid State Ion.* **1992**, *52*, 111–123. [[CrossRef](#)]
21. Kawada, T.; Watanabe, T.; Kaimai, A.; Kawamura, K.; Nigara, Y.; Mizusaki, J. High temperature transport properties in SrTiO_3 under an oxygen potential gradient. *Solid State Ion.* **1998**, *108*, 391–402. [[CrossRef](#)]
22. Hayashi, H.; Inaba, H.; Matsuyama, M.; Lan, N.G.; Dokiya, M.; Tagawa, H. Structural consideration on the ionic conductivity of perovskite-type oxides. *Solid State Ion.* **1999**, *122*, 1–15. [[CrossRef](#)]
23. Ohly, C.; Hoffmann-Eifert, S.; Szot, K.; Waser, R. Electrical conductivity and segregation effects of doped SrTiO_3 thin films. *J. Eur. Ceram. Soc.* **2001**, *21*, 1673–1676. [[CrossRef](#)]
24. Schmidbauer, M.; Kwasniewski, A.; Schwarzkopf, J. High-precision absolute lattice parameter determination of SrTiO_3 , DyScO_3 and NdGaO_3 single crystals. *Acta Cryst.* **2012**, *B68*, 8–14. [[CrossRef](#)] [[PubMed](#)]
25. Yaremchenko, A.A.; Brinkmann, B.; Janssen, R.; Frade, J.R. Electrical conductivity, thermal expansion and stability of Y- and Al-substituted SrVO_3 as prospective SOFC anode material. *Solid State Ion.* **2013**, *247–248*, 86–93. [[CrossRef](#)]
26. De Souza, R.A.; Ramadan, A.H.H. Ionic conduction in the $\text{SrTiO}_3 | \text{YSZ} | \text{SrTiO}_3$ heterostructure. *Phys. Chem. Chem. Phys.* **2013**, *15*, 4505–4509. [[CrossRef](#)] [[PubMed](#)]
27. Macias, J.; Yaremchenko, A.A.; Frade, J.R. Redox transition in strontium vanadates: Electrical conductivity and dimensional changes. *J. Alloys Compd.* **2014**, *601*, 186–194. [[CrossRef](#)]
28. Metlenko, V.; Ramadan, A.H.H.; Gunkel, F.; Du, H.; Schraknepper, H.; Hoffmann-Eifert, S.; Dittmann, R.; Waser, R.; De Souza, R.A. Do dislocations act as atomic autobahns for oxygen in the perovskite oxide SrTiO_3 ? *Nanoscale* **2014**, *6*, 12864–12876. [[CrossRef](#)]
29. Schie, M.; Waser, R.; De Souza, R.A. A Simulation Study of Oxygen-Vacancy Behavior in Strontium Titanate: Beyond Nearest-Neighbor Interactions. *J. Phys. Chem. C* **2014**, *118*, 15185–15192. [[CrossRef](#)]
30. Schulz, M.; Orland, T.; Mehlmann, A.; Rothschild, A.; Fritze, H. Oxygen transport in epitaxial $\text{SrTiO}_3/\text{SrTi}_{1-x}\text{Fe}_x\text{O}_3$ multilayer stacks. *J. Sens. Sens. Syst.* **2017**, *6*, 107–119. [[CrossRef](#)]
31. Liu, Z.T.Y.; Podraza, N.J.; Khare, S.V.; Sarin, P. Transparency enhancement for SrVO_3 by SrTiO_3 mixing: A first-principles study. *Comput. Mater. Sci.* **2018**, *144*, 139–146. [[CrossRef](#)]
32. Macias, J.; Yaremchenko, A.A.; Rodriguez-Castellon, E.; Starykevich, M.; Frade, J.R. Compromising Between Phase Stability and Electrical Performance: SrVO_3 - SrTiO_3 Solid Solutions as Solid Oxide Fuel Cell Anode Components. *ChemSusChem* **2019**, *12*, 240–251. [[CrossRef](#)] [[PubMed](#)]
33. Kolotygin, V.A.; Viskup, A.P.; Pivak, E.V.; Kharton, V.V. The Mixed Electronic and Ionic Conductivity of Perovskite-Like $\text{Ba}_{1-x}\text{Sr}_x\text{Fe}_{1-y}\text{Ti}_y\text{O}_{3-\delta}$ and $\text{BaTi}_{0.5}\text{Fe}_{0.5-z}\text{Ce}_z\text{O}_{3-\delta}$ Solid Solutions. *Russ. J. Electrochem.* **2020**, *56*, 110–117. [[CrossRef](#)]
34. Brese, N.E.; O’Keeffe, M. Bond-Valence Parameters For Solids. *Acta Cryst.* **1991**, *B47*, 192–197. [[CrossRef](#)]
35. Brown, I.D.; Poppelmeier, K.R. *Bond Valences*; Springer: Berlin, Germany, 2014.
36. Brown, I.D. *The Chemical Bond in Inorganic Chemistry: The Bond Valence Model*; Oxford University Press: Oxford, UK, 2016.
37. Gagné, O.C.; Hawthorne, F.C. Visualizing Lithium-Ion Migration Pathways in Battery Materials. *Acta Cryst.* **2015**, *B71*, 562–578.
38. Filsø, M.O.; Turner, M.J.; Gibbs, G.V.; Adams, S.; Spackmann, M.A.; Iversen, B.B. Visualizing Lithium-Ion Migration Pathways in Battery Materials. *Chem. Eur. J.* **2013**, *19*, 15535–15544. [[CrossRef](#)] [[PubMed](#)]
39. Gao, J.; Chu, G.; He, M.; Zhang, S.; Xiao, R.; Li, H.; Chen, L. Screening possible solid electrolytes by calculating the conduction pathways using Bond Valence method. *Sci. China Phys. Mech. Astron.* **2014**, *57*, 1526–1535. [[CrossRef](#)]
40. Inoue, R.; Fujii, K.; Shiraiwa, M.; Niwa, E.; Yashima, M. A new structure family of oxide-ion conductors $\text{Ca}_{0.8}\text{Y}_{2.4}\text{Sn}_{0.8}\text{O}_6$ discovered by a combined technique of the bond-valence method and experiments. *Dalton Trans.* **2018**, *47*, 7515–7521. [[CrossRef](#)]
41. Sale, M.; Avdeev, M. 3DBVSMAPPER: A program for automatically generating bond-valence sum landscapes. *J. Appl. Cryst.* **2012**, *45*, 1054–1056. [[CrossRef](#)]

42. Yamada, I.; Takamatsu, A.; Ikeno, H. Complementary evaluation of structure stability of perovskite oxides using bond-valence and density-functional-theory calculations. *Sci. Technol. Adv. Mater.* **2018**, *19*, 101–107. [[CrossRef](#)]
43. Lufaso, M.W.; Woodward, P.M. Prediction of the Crystal Structures of Perovskites Using the Software Program SPuDS. *Acta Cryst.* **2001**, *B57*, 725–738. [[CrossRef](#)]
44. Lufaso, M.W.; Barness, P.W.; Woodward, P.M. Structure prediction of ordered and disordered multiple octahedral cation perovskites using SPuDS. *Acta Cryst.* **2006**, *B62*, 397–410. [[CrossRef](#)] [[PubMed](#)]
45. Witten, I.H.; Frank, E.; Hall, M.A.; Pal, C.J. *Data Mining, Practical Machine Learning Tools and Techniques*, 4th ed.; Elsevier: Cambridge, MA, USA, 2017.
46. Witten, I.H.; Frank, E.; Hall, M.A.; Pal, C.J. *The WEKA Workbench*, 4th ed.; Morgan Kaufmann: Burlington, NJ, USA, 2016.
47. Kotthoff, L.; Thornton, C.; Hoos, H.H.; Hutter, F.; Leyton-Brown, K. Auto-WEKA 2.0: Automatic model selection and hyperparameter optimization in WEKA. *J. Mach. Learn. Res.* **2017**, *18*, 1–5.
48. Aha, D.; Kibler, D. Instance-based learning algorithms. *Mach. Learn.* **1991**, *6*, 37–66. [[CrossRef](#)]
49. Chang, C.-C.; Lin, C.-J. LIBSVM—A Library for Support Vector Machines. 2001. Available online: <http://www.csie.ntu.edu.tw/~cjlin/libsvm/> (accessed on 1 April 2022).
50. Yasser, E.-M. WLSVM. 2005. Available online: <http://www.cs.iastate.edu/yasser/wlsvm/> (accessed on 1 April 2022).
51. Liu, Y.; Zhao, T.; Ju, W.; Shi, S. Materials discovery and design using machine learning. *J. Mater.* **2017**, *3*, 159–177. [[CrossRef](#)]
52. Wang, A.Y.-T.; Murdock, R.J.; Kauwe, S.K.; Oliynyk, A.O.; Gurlo, A.; Brgoch, J.; Persson, K.A.; Sparks, T.D. Machine Learning for Materials Scientists: An introductory Guide toward Best Practices. *Chem. Mater.* **2020**, *32*, 4954–4965. [[CrossRef](#)]
53. Butler, K.T.; Davies, D.W.; Cartwright, H.; Isayev, O.; Walsh, A. Machine learning for molecular and materials science. *Nature* **2018**, *559*, 547–555. [[CrossRef](#)]
54. Schleder, G.R.; Padilha, A.C.M.; Acosta, C.M.; Costa, M.; Fazzio, A. From DFT to machine learning: Recent approaches to materials science—A review. *J. Phys. Mater.* **2019**, *2*, 032001. [[CrossRef](#)]
55. Schmidt, J.; Marques, M.R.G.; Botti, S.; Marques, M.A.L. Recent advances and applications of machine learning in solid-state materials science. *NPJ Comput. Mater.* **2019**, *5*, 83. [[CrossRef](#)]
56. Chen, C.; Zuo, Y.; Ye, W.; Li, X.; Deng, Z.; Ong, S.P. A Critical Review of Machine Learning of Energy Materials. *Adv. Energy Mater.* **2020**, *10*, 1903242. [[CrossRef](#)]
57. Xu, L.; Wencong, L.; Chunrong, P.; Qiang, S.; Jin, G. Two semi-empirical approaches for the prediction of oxide ionic conductivities in ABO_3 perovskites. *Comput. Mater. Sci.* **2009**, *46*, 860–868. [[CrossRef](#)]
58. Dai, D.; Liu, Q.; Hu, R.; Wei, X.; Ding, G.; Xu, B.; Xu, T.; Zhang, J.; Xu, Y.; Zhang, H. Method construction of structure-property relationships from data by machine learning assisted mining for materials design applications. *Mater. Des.* **2020**, *196*, 109194. [[CrossRef](#)]
59. Mistry, A.; Franco, A.A.; Cooper, S.J.; Roberts, S.A.; Viswanathan, V. How Machine Learning Will Revolutionize Electrochemical Sciences. *ACS Energy Lett.* **2021**, *6*, 1422–1431. [[CrossRef](#)]
60. Zhang, L.; He, B.; Zhao, Q.; Zou, Z.; Chi, S.; Mi, P.; Ye, A.; Li, Y.; Wang, D.; Avdeev, M.; et al. A Database of Ionic Transport Characteristics for Over 29,000 Inorganic Compounds. *Adv. Funct. Mater.* **2020**, 2003087. [[CrossRef](#)]
61. Pilania, G.; Balachandran, P.V.; Kim, C.; Lookman, T. Finding New Perovskite Halides via Machine Learning. *Front. Mater.* **2016**, *3*, 1–7. [[CrossRef](#)]
62. Balachandran, P.V.; Lin, L.; Anchell, J.S.; Bridges, C.A.; Ganesh, P. Defect Genome of Cubic Perovskites for Fuel Cell Applications. *J. Phys. Chem. C* **2017**, *121*, 26637–26647. [[CrossRef](#)]
63. Li, W.; Jacobs, R.; Morgan, D. Predicting the thermodynamic stability of perovskite oxides using machine learning models. *Comput. Mater. Sci.* **2018**, *150*, 454–463. [[CrossRef](#)]
64. Yamada, I.; Takamatsu, A.; Asai, K.; Shirakawa, T.; Ohzuku, H.; Seno, A.; Uchimura, T.; Fujii, H.; Kawaguchi, S.; Wada, K.; et al. Systematic Study of Descriptors for Oxygen Evolution Reaction Catalysis in Perovskite Oxides. *J. Phys. Chem. C* **2018**, *122*, 27885–27892. [[CrossRef](#)]
65. Xu, Q.; Li, Z.; Liu, M.; Yin, W.-J. Rationalizing Perovskite Data for Machine Learning and Materials Design. *J. Phys. Chem. Lett.* **2018**, *9*, 6948–6954. [[CrossRef](#)]
66. Li, J.; Pradhan, B.; Gaur, S.; Thomas, J. Predictions and Strategies Learned from Machine Learning to Develop High-Performing Perovskite Solar Cells. *Adv. Energy Mater.* **2019**, *9*, 1901891. [[CrossRef](#)]
67. Sun, S.; Hartono, N.T.P.; Ren, Z.D.; Oviedo, F.; Buscemi, A.M.; Layurova, M.; Chen, D.X.; Ogunfunmi, T.; Thapa, J.; Ramasamy, S.; et al. Accelerated Development of Perovskite-Inspired Materials via High-Throughput Synthesis and Machine-Learning Diagnosis. *Joule* **2019**, *3*, 1437–1451. [[CrossRef](#)]
68. Vieten, J.; Bulfin, B.; Huck, P.; Horton, M.; Guban, D.; Zhu, L.; Lu, Y.; Persson, K.A.; Roeb, M.; Sattler, C. Materials design of perovskite solid solutions for thermochemical applications. *Energy Environ. Sci.* **2019**, *12*, 1369–1384. [[CrossRef](#)]
69. Li, Z.; Najeeb, M.A.; Alves, L.; Sherman, A.Z.; Shekar, V.; Parilla, P.C.; Pendleton, I.M.; Wang, W.; Nega, P.W.; Zeller, M.; et al. Robot-Accelerated Perovskite Investigation and Discovery. *Chem. Mater.* **2020**, *32*, 5650–5663. [[CrossRef](#)]
70. Srivastava, M.; Howard, J.M.; Gong, T.; Dias, M.R.S.; Leite, M.S. Machine Learning Road map for Perovskite Photovoltaics. *J. Phys. Chem. Lett.* **2021**, *12*, 7866–7877. [[CrossRef](#)] [[PubMed](#)]
71. Tao, Q.; Xu, P.; Li, M.; Lu, W. Machine Learning for perovskite materials design and discovery. *NPJ Comput. Mater.* **2021**, *7*, 23. [[CrossRef](#)]

72. Park, H.; Ali, A.; Mall, R.; Bensmail, H.; Sanvito, S.; El-Mellouhi, F. Data-driven enhancement of cubic phase stability in mixed-cation perovskites. *Mach. Learn. Sci. Technol.* **2021**, *2*, 025030. [[CrossRef](#)]
73. Deng, Q.; Lin, B. Exploring structure-composition relationships of cubic perovskite oxides via extreme feature engineering and automated machine learning. *Mater. Today Commun.* **2021**, *28*, 102590. [[CrossRef](#)]
74. Chenebuah, E.T.; Nganbe, M.; Tchagang, A.B. Comparative analysis of machine learning approaches on the prediction of the electronic properties of perovskites: A case study of ABX_3 and $A_2BB'X_6$. *Mater. Today Commun.* **2021**, *27*, 102462. [[CrossRef](#)]
75. Sharma, A.; Kushvaha, V. Predictive modeling of fracture behavior in silica-filled polymer composite subjected to impact with varying loading rates using artificial neural network. *Eng. Fract. Mech.* **2020**, *239*, 107328. [[CrossRef](#)]
76. Sharma, A.; Mukhopadhyay, T.; Rangappa, S.M.; Siengchin, S.; Kushvaha, V. Advances in Computational Intelligence of Polymer Composite Materials: Machine Learning Assisted Modeling, Analysis and Design. *Arch. Comput. Methods Eng.* **2022**, *in press*. [[CrossRef](#)]
77. Alam, M.A.; Ya, H.H.; Azeem, M.; Yusuf, M.; Soomro, I.A.; Masood, F.; Shozib, I.A.; Sapuan, S.M.; Akhter, J. Artificial Neural Network Modeling to Predict the Effect of Milling Time and TiC Content on the Crystallite Size and Lattice Strain of Al7075-TiC Composites Fabricated by Powder Metallurgy. *Crystals* **2022**, *12*, 372. [[CrossRef](#)]
78. Gómez-Peralta, J.I.; García-Peña, N.G.; Bokhimi, X. Crystal-Site-Based Artificial Neural Networks for Material Classification. *Crystals* **2021**, *11*, 1039. [[CrossRef](#)]